ACS OMEGA

http://pubs.acs.org/journal/acsodf

Article

Tendon-Inspired Nanotopographic Scaffold for Tissue Regeneration in Rotator Cuff Injuries

Woochan Kim, Ga-Eon Kim, Mohamed Attia Abdou, Sujin Kim, Daun Kim, Sunho Park, Yang-Kyung Kim, Yonghyun Gwon, Sung-Eun Jeong, Myung-Sun Kim,* and Jangho Kim*

Cite This: *ACS Omega* 2020, 5, 13913−13925

Read Online

ACCESS | Metrics & More | Article Recommendations | Supporting Information

ABSTRACT: Acute and chronic rotator cuff (RC) tears are common etiologies of shoulder disabilities. Despite the advanced surgical techniques and graft materials available for tendon repair, the high re-tear rate remains a critical challenge in RC healing. Inspired by the highly organized nanotopography of the extracellular matrix (ECM) in tendon tissue of the shoulder, nanotopographic scaffolds are developed using polycaprolactone for the repair and regeneration of RC tendons. The scaffolds show appropriate flexibility and mechanical properties for application in tendon tissue regeneration. It is found that the highly aligned nanotopographic cues of scaffolds could sensitively control and improve the morphology, attachment, proliferation, and differentiation of tendon-derived cells as well as promote their wound healing capacity *in vitro*. In particular, this study showed that the scaffolds could promote tendon regeneration along the direction of the nanotopography in the rabbit models of acute and chronic RC tears. Nanotopographic scaffold-augmented rotator cuff repair showed a more appropriate healing pattern compared to the control groups in a rabbit RC tear model. We demonstrated that the tendon ECM-like nanoscale structural cues of the tendon-inspired patch may induce the more aligned tissue regeneration of the underlying tissues including tendon-to-bone interface.

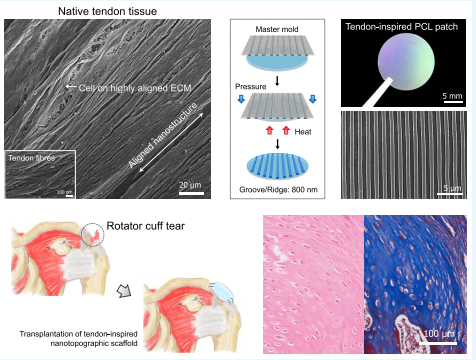

INTRODUCTION

Rotator cuff (RC) tears, which are caused mostly from the rupture of the tendons of the shoulder, are common etiologies of shoulder pain and disability.[1] In individuals of age ≥40 years, this type of tear can progress to a degenerative disease and then further to a chronic tear, with the prevalence ranging from 40 to 50% in patients ≥50 years of age.[2,3] RC tears can be treated by anti-inflammatory drugs, physical therapy, and rehabilitation therapy initially without the need for surgery. However, when these nonsurgical options fail, surgical intervention such as open or arthroscopic RC repairs are still recommended.[4−8] Despite the advanced surgical technique, some chronic massive RC tears are challenging entities to achieve tension-free complete repair at the footprint. Sometimes the footprint may not be covered completely by the repaired tendon so that the tendon-to-bone healing at the repair site would not be achieved successfully. The rates of re-tearing after surgical repair for a chronic RC tear are reportedly as high as 20−90%.[2,9−12] Therefore, the additional strategies to augment RC repair site by improving the mechanical integrity of repair site and/or biologic healing environment have been needed. Accordingly, various studies have been conducted to improve the RC tendon healing using strategies such as stem cells (*e.g.*, bone marrow-derived mesenchymal stem cells), stromal cells (*e.g.*, bone marrow-derived mesenchymal stromal cells and adipose-derived stromal cells), growth factors (*e.g.*, platelet-derived growth factor-BB and TGF-β1), platelet-rich plasma, and transplantable scaffolds (*e.g.*, chitosan fiber, collagen fiber, and PLGA/Col-PCL/*n*HA).[13−22] The augmentation using various scaffolds (*i.e.*, extracellular matrix (ECM)-derived scaffolds or synthetic polymer scaffolds) has been applied at the RC repair site to improve the tendon-to-bone healing as tissue engineering therapies. However, the current approaches still have several limitations in their efficiency to heal RC tears, especially in various aspects of their commercialization due to the limited availability of resources, poor regenerative capacity, low biocompatibility, and high cost.[23−25]

Cells living in the human body respond sensitively to the complex and well-organized microenvironment structures of the ECM, which may modulate the fate and functions of cells.[26−33] The well-defined organization and nanotopographic characteristics of the ECM might perform an important role in the regulation of the morphology, migration, proliferation, differentiation, and metabolism of cells.[28,34,35] In particular,

Received: March 25, 2020
Accepted: May 19, 2020
Published: June 2, 2020

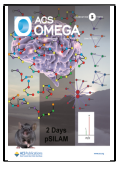

https://dx.doi.org/10.1021/acsomega.0c01328
ACS Omega 2020, 5, 13913−13925

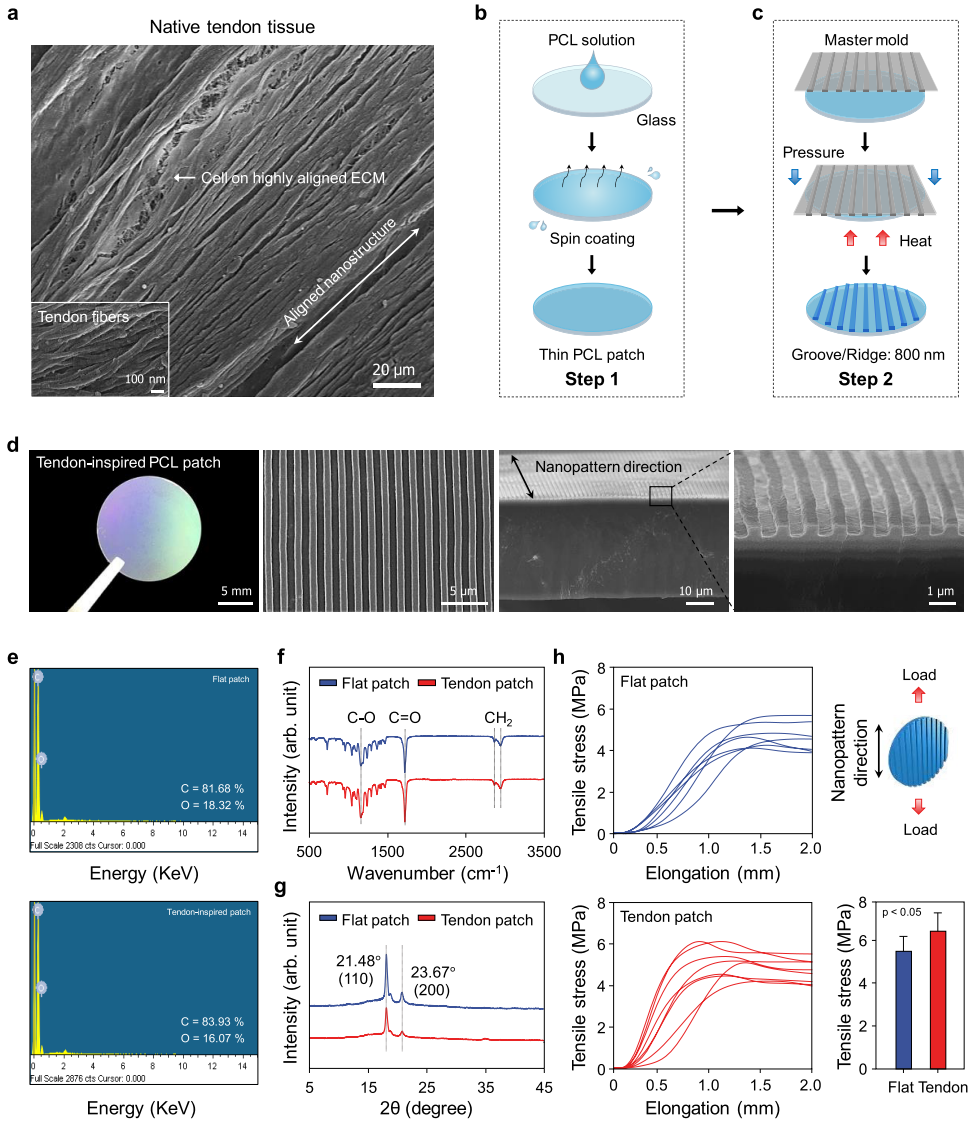

Figure 1. Design and fabrication of tendon-inspired scaffold. (a) Scanning electron microscopy (SEM) image of native RC tendon tissue of the rabbit. (b, c) Schematics for the fabrication of the tendon-inspired patches using spin-coating (step 1) and capillary force lithography (step 2). (d) Optical image and SEM images of the surface morphology and cross section of the tendon-inspired patch. (e) Energy-dispersive X-ray (EDX) analysis of the flat patch and tendon-inspired patch. (f) Fourier transform infrared (FT-IR) analysis of the flat patch and tendon-inspired patch. (g) X-ray diffraction (XRD) analysis of the flat patch and tendon-inspired patch. (h) Stress−strain diagram of the flat patch and tendon-inspired patch (n = 8 for each sample).

ECM in certain tissues (*e.g.*, skin, heart, bone, nerves, muscles, and tendons) has been widely observed to form a directional structure of tissues that exhibits anisotropic and geometric topography that affect tissue function.[27,29] Such unique organization is exhibited in the structure of natural tendon tissues, allowing them to act as fibrous connective tissues to connect muscles to bone (Figure 1a). Histologically, tendons consist of dense fascicles of regular connective tissue encased in dense sheaths of regular connective tissue. The ECMs of normal healthy tendons are composed mainly of parallel arrays of collagen fibers that are densely packed together. These collagen fibers range in size from fibrils of tens of nanometers to fibers of several hundred micrometers.[36] Thus, we hypothesized that the unique nanotopographical structural organization of the tendon ECM would be an important factor for regulating the morphology and function of cells as well as for the regeneration of tendon tissue.

Inspired by the high alignment and well-defined organization of the ECM of natural tendons, we designed a nanotopographic scaffold for use in the acceleration of tendon regeneration in acute and chronic rotator cuff healing. As a key design criterion for a more sophisticatedly structured ECM, the nanotopographically aligned matrix was developed using polycaprolactone (PCL) with capillary force lithography. Using this strategy, we investigated the influence of the nanotopographic cues on the morphology, adhesion, proliferation, differentiation, and wound healing ability of tendon-derived cells *in vitro*. Furthermore, using rabbit models of acute and chronic rotator cuff tears, we demonstrated that our newly developed scaffolds could promote tendon regeneration along the direction of the nanotopography.

https://dx.doi.org/10.1021/acsomega.0c01328
ACS Omega 2020, 5, 13913−13925

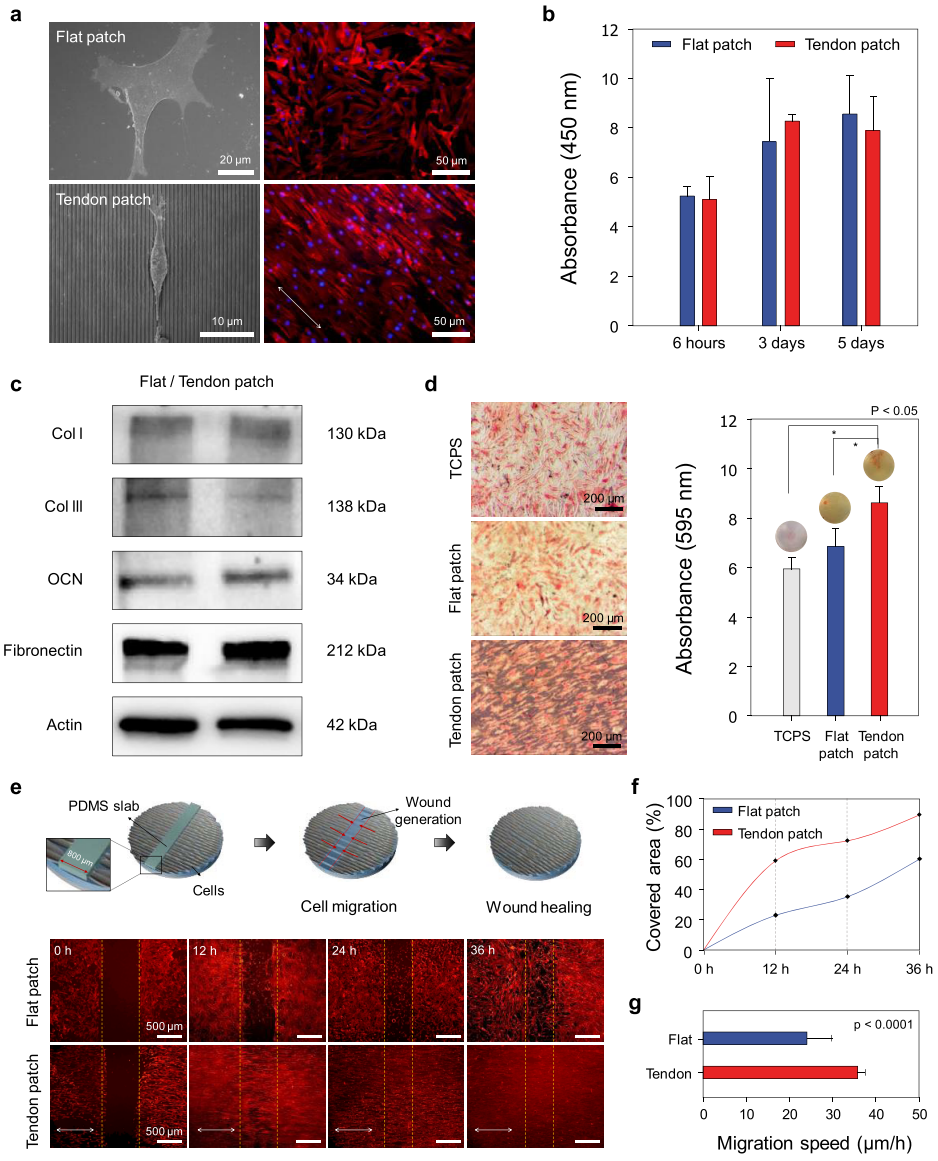

Figure 2. Effect of nanotopographic cues of tendon-inspired scaffold on the morphology, orientation, attachment, proliferation, differentiation, and wound healing activity of tendon-derived cells. (a) SEM images at the single-cell level, and immunofluorescence images of F-actin (red)- and 4,6-diamidino-2-phenylindole (DAPI) (blue)-stained tendon-derived cells at the multicell level on the flat patch and tendon-inspired patch. (b) Attachment (6 h) and proliferation (3 and 5 days) of cells on the flat patches and tendon-inspired patches. (c) Western blot analysis of collagen I (Col I), collagen III (Col III), osteocalcin (OCN), and fibronectin expression in tendon-derived cells cultured on the flat patches and tendon-inspired patches for 21 days. (d) Mineralization of tendon-derived cells by osteogenesis on the tendon-inspired patches. Alizarin red staining and quantification of the degree of osteogenesis revealed that the tendon-inspired patches promoted the greatest degree of mineralization of tendon-derived cells compared to the flat patches and the tissue culture polystyrene substrate (TCPS). (e) Experimental procedure of the *in vitro* wound healing study using poly(dimethylsiloxane) (PDMS) slabs (width: 800 nm), and the wound healing process. Immunofluorescence images (F-actin in red) of *in vitro* wound healing with respect to the orientations of the nanotopography at 0, 12, 24, and 36 h. (f) Quantification of the area covered by tendon-derived cells on the flat patches and tendon-inspired patches. (g) Migration speed analysis according to topographic features of the flat patches and tendon-inspired patches.

RESULTS AND DISCUSSION

Design and Fabrication of Tendon-Inspired Scaffolds.

Anatomically, the RC consists of four tendon groups: supraspinatus, infraspinatus, teres minor, and subscapularis. The tendon tissue is a fibrous connective tissue that usually connects muscles to bone and is capable of withstanding tension. Normal tendons are composed of well-organized and highly aligned collagen fibers in a matrix rich with approximately 86% collagen of mainly type I and small amounts of type III. These fibers exist in closely packed parallel arrays that are cross-linked with proteoglycans.[37] In tendons, a collagen fiber consists of a large number of fibrils. The diameter of collagen fibrils, which assemble to form collagen fiber, varies from 500 nm to 1 μm. The collagen fibers assemble to form bundles (or fascicles) of approximately 10 mm in length and 1−20 μm in diameter. These fiber bundles finally assemble to form a tendon unit with a diameter of 20−500 μm.[36,37] The tendon-derived cells reside mainly in between the collagen fibers and are affected by the collagen structure. To confirm the existence of these well- and highly aligned collagen fibers and nanoscaled ECM in the tendon, an *ex vivo* study was carried out using uninjured rabbit tendon

https://dx.doi.org/10.1021/acsomega.0c01328
ACS Omega 2020, 5, 13913−13925

tissue. Figure 1a shows the highly aligned collagen fibers with a diameter of approximately 800 nm, suggesting that they may be able to provide specific nanotopographic cues for guiding the fate and function of tendon-derived cells in ECMs during tendon repair or regeneration. Thus, we manipulated nanopographic structures onto PCL-based scaffolds inspired by anisotropic nanostructure of the collagen fiber of the native tendon ECM.

Capillary force lithography was applied to fabricate PCL-based nanotopographically aligned scaffolds with tunable topographic structures and sizes similar to those of the well-organized nanotopographic ECM of tendon tissue (Figure 1b,c). For efficient control of the nanotopographic structures on PCL, a thin-layered PCL patch was first fabricated by spin-coating the polymer onto a circular glass (Figure 1b). Because solvent evaporation during the spin-coating process had caused the surface of the thin-layered PCL patch to become irregularly structured, a flat-surfaced poly(dimethylsiloxane) (PDMS) mold was used to flatten the PCL surface into even topographic structure. To fabricate highly aligned nanotopography on the PCL patch, the PDMS mold with a nanotopographic surface (ridges and grooves: 800 nm; depth: 500 nm) was prepared. Finally, using the flat-surfaced and nanotopographic PDMS molds, flat and nanotopographic PCL scaffolds (hereafter referred to as the "flat patch" and "tendon-inspired patch," respectively) were fabricated by applying the heat and pressure of the capillary force−soft lithography process. Figure 1b,c shows a schematic of the scaffold fabrication process developed in this study (described in detail in the Experimental Section).

Scanning electron microscopy (SEM) images of the surface morphology of the tendon-inspired patch revealed a highly aligned nanotopography with grooves and ridges, similar to the well-organized and highly aligned nanotopography of the tendon ECM (Figure 1d). As shown in the cross-sectional SEM images of the tendon-inspired patch, the topography had nanoscale ridges and grooves (800 nm; depth: 500 nm) of 30 μm thickness. To verify whether the heat and pressure used in the soft lithography process had changed the PCL properties, the polymer's chemical characteristics were analyzed. Energy-dispersive X-ray spectroscopy (EDS) detected approximately 80% carbon and 20% oxygen elements in the PCL matrix, without significant difference between the flat and tendon-inspired patches (Figure 1e). The functional groups of both types of scaffolds were investigated by Fourier transform infrared (FT-IR) spectroscopy. The characteristic absorption bands related to PCL (*i.e.*, CH_2 asymmetric stretching at 2944 cm^{-1}, symmetric stretching at 2866 cm^{-1}, C=O stretching vibration of carbonyl groups at 1721 cm^{-1}, and deformation of C−O at 1161 cm^{-1}) were detected in both scaffolds (Figure 1f), indicating that the functional groups were well maintained and had been unaffected by the heat and pressure used. We further investigated the crystallinity of the scaffolds by X-ray diffraction (XRD) spectroscopy. The strong and sharp crystalline peaks (Figure 1f) observed at 21.48 and 23.67° are attributed to the [110] and [200] crystallographic planes of the PCL crystal, respectively, indicating that the flat and tendon-inspired patches had been successfully fabricated without variation in the specific crystalline structures of pure PCL. The tensile strengths of the two types of scaffolds were measured using a tensile tester and assessed if the torn tendon tissue could be mechanically supported by the aligned nanotopographic patch after RC tear surgery. Interestingly, when a load was applied along the direction of the aligned topography, the nanotopography displayed a larger tensile stress (~6.47 MPa) than that (~5.42 MPa) of the flat topography (Figure 1h). The tendon-inspired patches displayed Young's modulus (69.18 MPa), breakpoint stress (4.18 MPa), and breakpoint strain (78%), whereas Young's modulus (42.68 MPa), breakpoint stress (3.55 MPa), and breakpoint strain (73%) of the flat patches were observed (Figure S1). Overall, the mechanical properties of the tendon-inspired nanotopographic patches were improved compared to those of the flat patches. Our results demonstrated that the tendon-inspired nanotopographic patch was successfully fabricated as an efficient scaffold maintaining the properties of the PCL.

***In Vitro* Study.** Nanotopographic cues are known as important regulators of living cell and tissue function.[38] To investigate the effects of the nanotopographic cues on cellular structures at the single-cell level, the morphologies and orientations of tendon-derived cells on the tendon-inspired patch were observed by SEM. The nanotopographic cues greatly influenced the polarity of the tendon-derived cells, as evidenced by the alignment of the cytoskeletal structure in response to the highly aligned nanotopography (Figure 2a). After 12 h of culture, the tendon-derived cells were well attached onto both the flat and tendon-inspired patches (Figure 2b). However, the tendon-derived cells on the flat topography exhibited a random shape and orientation, whereas those on the nanotopography showed a highly aligned and oriented morphology. After 3 days of culture, the effects of the nanotopographic cues on the shape, organization, and orientation of the tendon-derived cells were evaluated at the multicell level using immunofluorescence staining. The immunofluorescence images showed that the tendon-derived cells had adhered to the flat patch and were randomly spread. In contrast, on the tendon-inspired patch, the tendon-derived cells had a highly aligned cell shape and well-organized cell−cell interactions and were aligned in the direction of the nanotopography, similar to natural tendon ECMs. Taken together, our results indicate that the tendon ECM-inspired nanotopography could strongly influence the alignment and shape orientation of tendon-derived cells to coincide precisely with the natural orientation of cells *in vivo*.

To investigate whether the nanotopographic cues of the scaffolds influence cell attachment (6 h) and proliferation (5 days), we cultured tendon-derived cells on the flat (control group) and tendon-inspired patches *in vitro*. After 6 h of cell culture, the cells attached onto the scaffolds were quantified by WST assay. The tendon-derived cells were well attached onto the tendon-inspired patches compared to the flat topographical patches (Figure 2b). After 5 days of cell culture, cell proliferation was higher on the tendon-inspired patches than on the flat topography. These results indicate that the aligned nanotopographic structure may provide the suitable environment for attachment and proliferation of tendon-derived cells.

Because RC tears most often result from avulsion of the supraspinatus tendon from the humeral head at the tendon insertion site, the insertion of normal tendon into the bone for regeneration is required.[39] The supraspinatus tendon integrates into the humeral head *via* the direct enthesis, which is a multizonal interface that exhibits region-dependent matrix heterogeneity and consists of a gradient of mineral content, namely, the tendon, nonmineralized fibrocartilage, mineralized fibrocartilage, and bone.[39] Therefore, gene expression of ECM-

https://dx.doi.org/10.1021/acsomega.0c01328
ACS Omega 2020, 5, 13913−13925

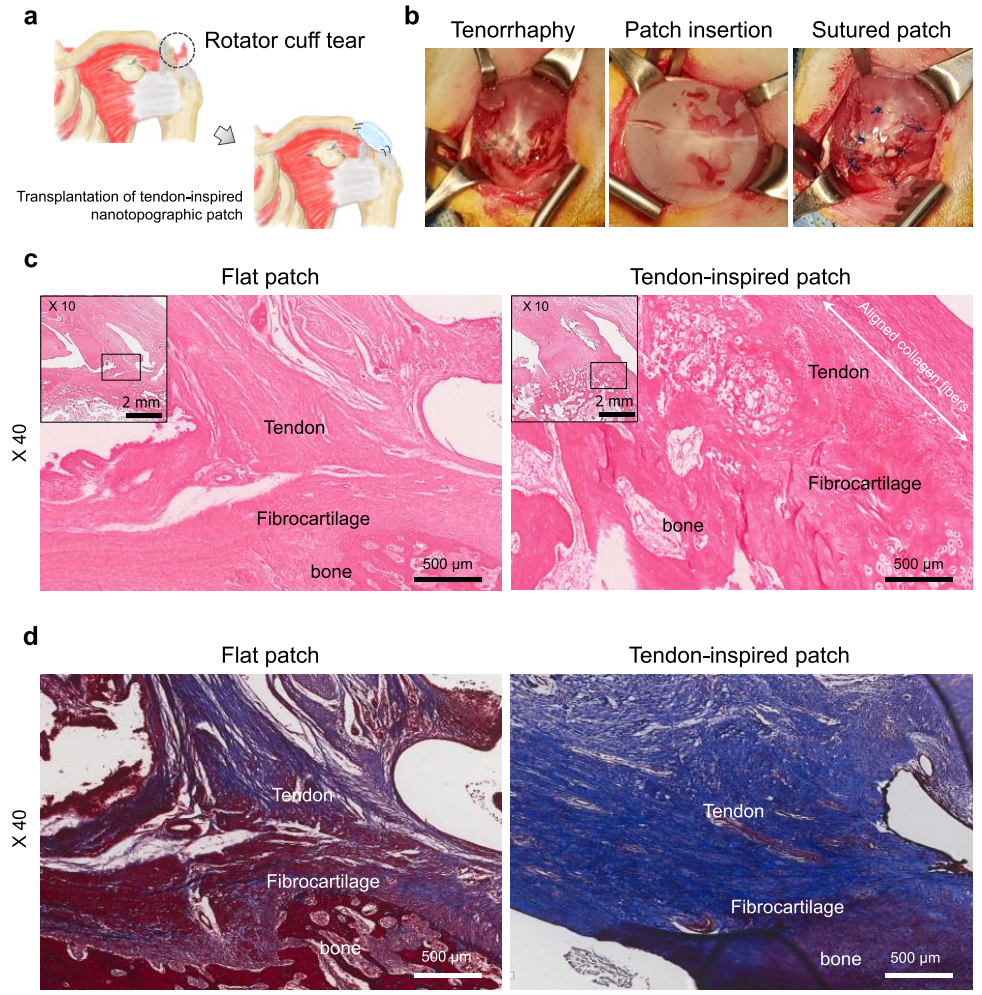

Figure 3. Surgical procedure and *in vivo* animal study using a rabbit model of acute RC tears. (a) Schematic of the transplantation of a tendon-inspired patch. (b) Surgical procedure for RC tendon repair using a tendon-inspired patch. The tendon-inspired patches were grafted onto the defected tendon tissue after tenorrhaphy of the torn RC tendon. (c) Representative histologic images by hematoxylin and eosin staining and (d) representative histologic images by Masson's trichrome staining of the flat patches and tendon-inspired patches insertion site onto the supraspinatus tendon after 6 weeks of repair. Representative images of the insertion site after application of the patches (n = 6 for each sample).

related proteins and osteogenic mineralization to regenerate mineralized fibrocartilage onto the bone is important for repair of the mechanical properties and function of the RC. Accordingly, Western blot analysis was conducted to better demonstrate the effect of the tendon ECM-like nanotopography by determining the expression of molecules related to tendon-derived cells differentiation. The results showed upregulation of collagen type I, osteocalcin, and fibronectin on the tendon-inspired patch relative to that on the flat scaffolds. In contrast, collagen type III was slightly downregulated on the tendon-inspired patches (Figures 2c and S2). In addition, we examined the osteogenic mineralization of tendon-derived cells on the nanotopography by culturing the cells on tendon-inspired patches in osteogenic induction medium for 14 days. Alizarin Red staining (Figure 2d) revealed higher calcium expression levels on the nanotopography than on both the flat topography and the tissue culture polystyrene substrate (TCPS). Quantification of the osteogenic mineralization on the three substrates also demonstrated the highest degree of osteogenesis by the cells on the nanotopography. These findings suggest that the tendon ECM-like nanotopography promoted osteogenic mineralization and collagen type I, which may play important roles in tendon and fibrocartilage regeneration.

In general, wound healing is governed by two distinct cell behaviors: migration and proliferation.[29] To evaluate the effect of aligned nanotopography cues of our scaffolds on tendon wound healing, we prepared a wound healing system as an *in vitro* model by creating cell-free areas on the scaffolds. Figure 2e illustrates an experimental design for the wound healing system. Thin PDMS slabs were first placed onto the surfaces of the flat and tendon-inspired patch. Then, tendon-derived cells were seeded onto the patches and cultured until a confluent monolayer had formed. The PDMS slabs were then carefully removed, and the migration and proliferation of cells into the cell-free areas were observed and analyzed independently at every 12 h (0, 12, 24, and 36 h). The cell-free areas (wound generation) of approximately 800 μm in width had formed at 0 h (Figure 2e). At 36 h, the tendon-derived cells on the flat patch had not completely covered the cell-free areas. In contrast, at 24 h, the tendon-derived cells on the tendon-inspired patch had completely covered the cell-free areas, and it was observed that the cells were moving so that the artificial wound area was indistinguishable at 36 h. Importantly, the repaired wounds on the nanotopography exhibited morphol-

https://dx.doi.org/10.1021/acsomega.0c01328
ACS Omega 2020, 5, 13913−13925

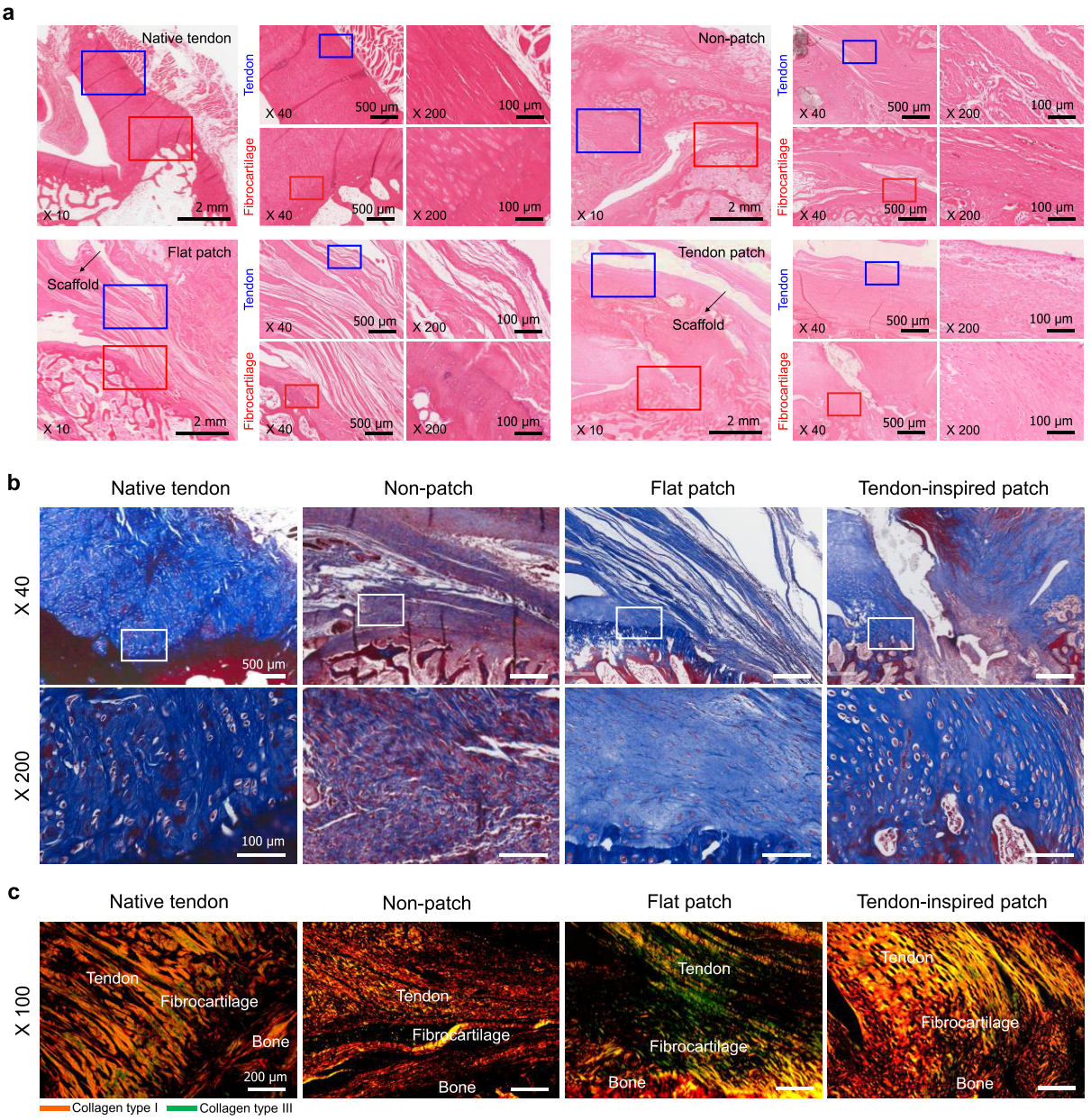

Figure 4. *In vivo* animal study using a rabbit model of chronic RC tears. (a) Representative histologic images (H&E staining) of native tendon tissues, nonpatches, the flat patches, and tendon-inspired patch groups. The increase in the parallel alignment of collagen fibers was similar to that of native tendon tissue. Restoration of the native tissue microenvironment, including the parallel alignment of tendinous collagen and persistence of the fibrocartilage layer homogeneity, was observed to be increased on the tendon-inspired patches (n = 3 for each sample). (b) Representative histologic images (Masson's trichrome) of the patch insertion site onto the supraspinatus tendon after 6 weeks of repair, using rabbits in which chronic injury had been left unattended for 4 weeks. (c) Representative histologic images (Picrosirius red staining) of chronic RC tendon tissue repaired using tendon-inspired patch. Aligned fiber structures of collagen type I (orange color) and collagen type III (green) of native RC tendon tissue and RC tendon tissue repaired using tendon-inspired patch and control groups (nonpatch and flat patch).

ogy such as the highly aligned nanotopography and parallel anisotropic collagen fibers in a complex network of cells and surrounding ECM. These results were further quantified, where consistently more areas were covered by cells on the nanotopography than on the flat topography over time (Figure 2f). The orientation of the nanogrooves and ridges had also significantly affected the cell migration speed, which (36 μm/h) was faster on the tendon-inspired patch than on the flat patch (24 μm/h) (Figure 2g). Thus, our results demonstrated a notable influence of the nanotopography in the wound healing process: (i) the nanotopographic cues significantly promoted the migration of the tendon-derived cells into the wound area; (ii) the orientation of the nanotopography significantly affected the migration speed of the tendon-derived cells; and (iii) the tendon-inspired patch provided an efficient environment for constructing the structure of the native tendon ECM in which tendon-derived cells could proliferate and migrate into the wound area.

***In Vivo* Animal Study.** All rabbits used in the *in vivo* studies survived up to the designated sacrifice date, and no adverse events were observed. Figure 3a,b shows a process of transplantation of tendon-inspired patch at the RC repair site. The flat and tendon-inspired patches (diameter: 25 mm) were then respectively grafted onto the defects during 6 weeks after

https://dx.doi.org/10.1021/acsomega.0c01328
ACS Omega 2020, 5, 13913−13925

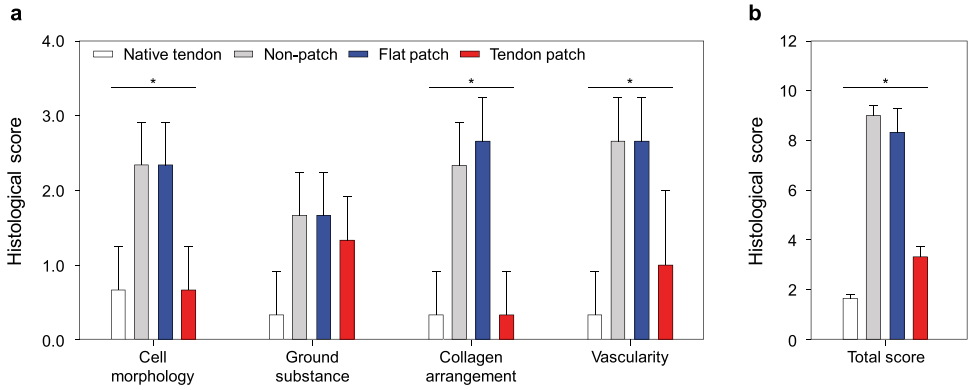

Figure 5. Semiquantitative analysis of the histological evaluation scores on repaired tendon-to-bone interfaces of chronic RC tear animal models. Native tendon (n = 3), nonpatch (n = 3), flat patch (n = 3), and tendon-inspired patch (n = 3) groups were evaluated using histologic images after 6 weeks of repair. (a) Histological scores for cell morphology, ground substance, collagen arrangement, and vascularity. (b) Total histological score on the sum of four variables. *P < 0.05.

acute supraspinatus tendon tear creation. No infection, contracture, mobility disability, or inflammatory reaction was observed in any of the rabbits throughout the postoperative period. Macroscopically, all of the RC repair sites implanted with the patches were covered with smooth connective tissue at 6 weeks after surgery.

To confirm the healing efficacy of the nanotopographic cues, hematoxylin and eosin (H&E) staining and Masson's trichrome staining were performed and evaluated the histologic quality (*i.e.*, connection of collagen fibers in the tendon−bone interface, orientation and density of the collagen fibers, maturity of the tendon−bone interface, blood vessel density, and cell confluency) at RC repair site after 6 weeks of repair with the patches. The RC tendon repaired using the tendon-inspired patch showed well-organized collagen fibers with a high density compared to that repaired using the flat patch in condition of acute RC tear model (*i.e.*, the flat and tendon-inspired patches were transplanted after tenorrhaphy immediately after supraspinatus tendon tear) (Figure 3c). The fibrocartilage tissues at tendon-to-bone interfaces treated with the tendon-inspired patch showed well-organized vertical arrangement compared to the flat scaffold group (Figure 3d). However, the flat patch group showed that fat metamorphosis did not improve at the area where the flat support was attached, and the fibrous tissue and cell density at the bone and fibrocartilage area showed a less histologic pattern (Figure 3d).

To evaluate the efficacy of the tendon-inspired patch in repairing a chronic RC tear, we prepared a chronic RC tear model of a rabbit by sharp release of the supraspinatus tendon at the greater tuberosity of the humeral head. First, we confirmed the chronicity of the RC tear with time (before scaffold insertion) in the rabbit model by creating supraspinatus tendon tear and observing the degree of fatty degeneration of the supraspinatus muscles at 2, 4, 6, 8, and 12 weeks. To evaluate the fatty degeneration of the RC muscles, Goutallier fatty degeneration staging was used, that is, stage 0: completely normal tendon without any fatty streaks; stage 1: the tendon contains some fatty streaks; stage 2: the amount of tendon is greater than that of fatty infiltration; stage 3: the amount of tendon is equal to that of fatty infiltration; and stage 4: the amount of fatty infiltration is greater than that of the tendon. The chronic tears showed increased fatty degeneration with increasing time, being at higher than stage 2 after 6 weeks. This verified our successful development of a rabbit model of chronic RC tears. The detailed method and results have already been reported by our group.[40]

Next, we grafted the flat and tendon-inspired patches onto the chronic defects at 4 weeks after tendon tear creation, respectively. The nonpatch group was sutured without any scaffold at 4 weeks after tendon tear creation. We then observed the regeneration of the repaired tendon at 6 weeks by histologic evaluation. Both engrafted patches were confirmed to be biocompatible, adapting well to the host tissue without any foreign body reaction at the attachment site. Interestingly, the rabbits treated with the tendon-inspired patch showed well-organized and highly aligned collagen fibers of a high density at the section under the scaffolds, whereas the nonpatch control and flat patch groups showed sparse fibrous tissue and low cell confluency (Figure 4). Importantly, the tendon-inspired patch group showed more superior and native tendon-to-bone healing patterns at the repair site compared to the nonpatch control and flat patch groups (Figure 4a). The fibrocartilage tissues at the tendon-to-bone interface of the tendon-inspired patch group showed the vertical arrangement similar to the native fibrocartilage, whereas the nonpatch control and flat patch groups showed less native histologic pattern (Figure 4b).

To demonstrate the effects of tendon-inspired patch on tendon tissue regeneration, picrosirius red staining images under polarized light at the fibrocartilage of the tendon−bone interface were observed, showing the different collagen fiber contents at the repair site (Figure 4c). It was clearly observed that the tendon-inspired patch could promote the organization of tendon tissues with dense property compared to the nonpatch group and the flat patch group. Furthermore, the enhanced expression of type I collagen fibers (yellow color) was observed at the fibrocartilage section repaired using tendon-inspired patch compared to those of other groups. These results demonstrated that the tendon-inspired patch significantly improved the tendon-to-bone healing, dense organization of collagen fiber, and production of type 1 collagen at tendon-to-bone interface. Thus, the nanotopographical cue of tendon-inspired patch had obviously influenced the collagen organization, connection, and tendon tissue regeneration as structure similar to native RC tendon tissues and fibrocartilage tissues at the tendon-to-bone interface. Based on the qualitative histologic analysis on the effect of tendon-inspired patch presented as a strategy for

https://dx.doi.org/10.1021/acsomega.0c01328
ACS Omega 2020, 5, 13913−13925

repair of chronic RC tendon tear, the semiquantitative histology analysis was performed using the Bonar scoring system (Figure 5 and Table S1). Cell morphology, ground substance, collagen arrangement, and vascularity changes were observed in all groups and were graded depending on the Bonar score (Table S2). The cell morphology and collagen arrangement scores of the tendon-inspired patch group were evaluated like those of the native tendon group and were significantly lower than those of the nonpatch and flat patch groups (Figure 5a). Generally, it was confirmed that there was no significant difference between the nonpatch and flat patch groups on all variables. The ground substance and vascularity scores of the tendon-inspired patch group were slightly higher than those of the native tendon group but were significantly lower than those of the nonpatch and flat patch groups. Overall, the total histological score of the tendon-inspired patch group was slightly higher than that of the native tendon group and significantly lower than those of the nonpatch and flat patch groups (Figure 5b). These results indicate the importance of a precisely aligned nanotopography in synthetic ECMs for guiding tendon tissue and fibrocartilage regeneration.

During the last decade, various platforms based on natural and synthetic biomaterials have been proposed as scaffolds for the augmentation of RC repair and tendon healing. Scaffolds such as Restore, CuffPatch, GraftJacket, TissueMend, and Zimmer Collagen Repair, which are made from natural biomaterials derived from the mammalian extracellular matrix (ECM) (*e.g.*, the dermis of humans and animals, and the small intestinal submucosa) have been widely used as graft platforms for repair of the RC tendon in the clinical setting. The Young's modulus of the human supraspinatus tendon usually has an approximate range of modulus values of 10−140 and 45−170 MPa.[23,41] The tendon-inspired patches displayed a Young's modulus of 69.18 MPa. GraftJacket, TissueMend, Restore, and CuffPatch, which were commercially available extracellular matrix scaffolds for rotator cuff tendon repair, exhibited linear moduli of approximately 22, 15, 35, and 40 MPa, respectively.[42,43] However, these ECM-derived scaffolds were a poor remodeling of the ECM and showed significantly lower mechanical strength than that of the natural tendon tissue owing to their propensity to biodegrade rapidly before the tendon and fibrocartilage have had a chance to fully regenerate.[23,41−45] Therefore, we hypothesized that the tendon-inspired patch would be successfully supported during the repair period after transplantation due to the better mechanical strength and long biodegradation period compared to the ECM-derived scaffolds.

In this study, we chose the PCL polymer for the tendon-inspired patch because of its suitability for tissue engineering and application in the biomedical fields: (i) PCL is degraded into water and carbon dioxide by hydrolysis of its ester linkages in physiological conditions.[42,43,46] Thus, PCL is a biocompatible polymer approved by the FDA for specific application in the human body. (ii) It is one of the most widely used polymers for biomedical applications owing to its controllable biodegradability within several months to several years, depending on the molecular weight, degree of crystallinity of the polymer, and conditions of degradation.[45,47,48] PCL has the capacity to promote the formation of new tissues and degrades along with tissue regeneration, while supporting and positioning the defects, and is thus a suitable material for replacing or treating damaged tissues. (iii) It has good flexibility and robust mechanical properties. (iv) It is easy to process and is relatively inexpensive compared to other biocompatible and biodegradable polymers, making it suitable for commercialization. However, although PCL is a biocompatible and biodegradable material, its poor bioactivity (related to the absence of bioactive functional groups on the surface) and low surface energy clearly reduce the cell affinity and inhibit cellular interactions, leading to low tissue regeneration rates. To overcome the low bioactivity of PCL, we fabricated surface-modified nanotopographic scaffolds by employing nanofabrication to improve the affinity and bioactivity of cells. Thus, in addition to the fact they would be structurally rigid and flexible enough to support the recovering tendons, we fabricated nanotopographic patches using PCL to ensure that they would not have to be removed over a long term before full tissue regeneration.

It is known that the behaviors and functions of cells are sensitively controlled by ECM-like topographic cues (*i.e.*, precisely defined micro- and nanostructures).[26,28,31,38,49] Our *in vitro* and *in vivo* study also demonstrated the effect of highly aligned nanotopographic cues on the enhanced behaviors and functions of tendon-derived cells. In particular, the cytoskeletal morphology of the tendon-derived cells at the multicell level showed them to be highly aligned and oriented with the dense actin filaments, inducing dense and well-organized collagen fibers for tendon regeneration. On the basis of our study, we propose other potential applications of the PCL-based tendon-inspired patch for biomedical applications. This patch or technology may allow the fabrication of precisely defined nanotopographic and microtopographic substrates for use in tendon tissue regeneration in various organs (*e.g.*, Achilles tendon, patellar tendon, and tennis elbow tendon). Recently, stem cell-based therapy has been highlighted as another strategy for maximizing the regeneration of tendon of RCs.[15,50,51] Accordingly, our tendon-inspired patch could be integrated with this stem cell platform to control and enhance the stem cell behaviors and functions as well as prevent their loss in the targeted tissue area.

In this work, we tried to show the possibilities on the effects of new scaffolds for tissue regeneration in rotator cuff injuries in animal models (Figures 3 and 4). Since we showed some important evidence about the performance of scaffolds (*e.g.*, histological observation and evaluation) in the current work, it is needed to perform the detailed *in vivo* study (*e.g.*, large animal models, biomechanical tests, *etc.*) using our proposed scaffolds, especially toward their clinical applications.

CONCLUSIONS

In this study, inspired by the high alignment and microenvironment of the native tendon ECM, tendon-inspired nanotopographic patches were developed as a means of controlling tendon-derived cells behavior and healing of RC tendon tissue. The precisely defined tendon-inspired patches were fabricated *via* capillary force lithography in combination with the spin-coating method using the PCL polymer. We demonstrated that the tendon ECM-like nanoscale structural cues of the tendon-inspired patch could improve cellular behaviors and tissue regeneration. The tendon-inspired patches promoted the tendon tissue repair and regeneration in both the *in vivo* models of acute and chronic RC tears. Although an in-depth study is still needed to elucidate the mechanisms underlying the nanotopographic cues for the tendon tissue regeneration, our current study provides new insight not only

https://dx.doi.org/10.1021/acsomega.0c01328
ACS Omega 2020, 5, 13913−13925

for shoulder tendon tissue repair and regeneration but also for various other tendons based on FDA-approved biomaterials as new medical devices.

EXPERIMENTAL SECTION

Preparation and Observation of *Ex Vivo* Rabbit Tendon Tissue. The detailed method to prepare *ex vivo* tissue has already been reported by our group.[49] Tendon tissue was obtained from rabbit surgery for tear model resected right supraspinatus tendon. Tendon tissue was fixed overnight with a solution containing 2% glutaraldehyde, 0.1 M sodium cacodylate, and 3 mM calcium chloride (pH 7.4) at 4 °C. The tendon tissue was rinsed three times with phosphate-buffered saline (PBS). The specimen was perfused with 1% osmium tetroxide and placed on a tissue rotator for 30 min. The sample was then rinsed in PBS three times. The tissue was serially dehydrated in 50, 70, 90, 95, and 100% of acetone. Each specimen was treated with hexamethyldisilazane (HMDS), air-dried, and placed on a stub for sputter coating with platinum. The tissue was then observed with a field emission scanning electron microscope (FE-SEM, ZEISS GeminiSEM 500, Germany).

Fabrication of Nanotopographic Poly(urethane acrylate) (PUA) Mother Mold and Poly(dimethylsiloxane) (PDMS) Mold. The detailed method to fabricate PUA mold has already been reported by our group.[49] A droplet of UV-curable PUA (Changsung Sheet., Korea) precursor solution with photoinitiator was dropped on the silicon master mold, on which nanosized linear grooves and ridge (800 nm) were etched using conventional photolithography and reactive ion etching. The mold was then uniformly covered with a poly(ethyleneterephthalate) (PET) film utilizing capillary force. After the master mold was exposed to UV light (λ = 352 nm, 40 W) for 60 s, the cured nanotopographic PUA replica was peeled off from the master mold using tweezers and again exposed to UV light for overnight to completely annihilate any residual reactive acrylate groups. First, nanotopographic PUA mother mold (800 nm ridges and grooves) was attached into a Petri dish with the surface of nanotopography facing up. Poly(dimethylsiloxane) (PDMS) prepolymer (Sylgard 184 Silicon Elastomer, Dow Corning) was mixed with 15% curing agent, poured onto the PUA mother mold in a Petri dish to a sufficient thickness (~1 cm), and baked at 70 °C for at least 6 h to ensure curing without any residue. The cured nanotopographic PDMS mold (800 nm ridges and grooves) was then peeled off from PUA mother mold in the Petri dish. To fabricate the flat patch as the control group, flat silicon wafer was attached into the Petri dish with the flat surface of silicon wafer with facing up. Then, as same fabrication protocol of nanotopographic PDMS mold, PDMS prepolymer (Sylgard 184 Silicon Elastomer, Dow Corning) was mixed with 15% curing agent, poured onto the flat Si wafer in a Petri dish to a sufficient thickness (~1 cm), and baked at 70 °C for at least 6 h to ensure curing without any residue. The cured flat PDMS mold (800 nm ridges and grooves) was then peeled off from the flat PUA mother mold in the Petri dish.

Design and Fabrication of Tendon-Inspired Patch. Polycaprolactone particles (PCL, M_w: 80 000; Sigma-Aldrich) was dissolved in dichloromethane using a magnetic stirrer, and a PCL solution of 18 wt % (w/w) in dichloromethane was prepared. The thin PCL patch was fabricated by spin-coating the PCL solution and then pouring it onto a 1.5 mm circular glass on the vacuum chuck of a spin coater. The spin-coating condition was as follows: rotator speed, 3500 rpm; duration time, 120 s; and acceleration time, 5 s. First, we fabricated a flat patch because the surface of the spin-coated PCL patch has irregular roughness of surface for the fabrication of nanotopographic PCL patches and utilization of the control group. The fabricated thin PCL patch was placed onto the silicon wafer substrate to melt the PCL layer with facing up on the hot plate for 60 s at 80 °C. The flat or nanotopographic PDMS (800 nm ridges and grooves) mold was placed on the premelted PCL layer and embossed onto the melted PCL layer by applying the pressure of smooth finger force while heating at 80 °C for 2 min. After the thermal imprinting process, the assembly of the PCL layer on circular glass and PDMS molds was cooled at room temperature for 30 min, and the PDMS mold was peeled off from the PCL layer on a circular glass resulting tendon-inspired patch with 800 nm ridges and grooves. The tendon-inspired patch was separated from the circular glass by washing 70% ethanol to insert only the patch without glass into the animal body.

Morphological Property of Tendon-Inspired Patch. High-resolution field emission scanning electron microscopy (FE-SEM) images of surface and cross section of tendon-inspired patches and flat patch were observed using a JSM-7500F microscope (Oxford, U.K.) at an acceleration voltage of 15.0 kV and an average working distance of 8.8 mm. The cross sections of the patches were prepared by cutting vertically along the pattern direction by quick freezing using liquid nitrogen for 5 min. Finally, the samples were coated with platinum prior to morphology observation of the samples.

Chemical Characteristics of Tendon-Inspired Patch. The chemical characteristics of flat and tendon-inspired patches were analyzed to confirm the chemical variation of the samples. The atomic composition of the samples was analyzed by an energy-dispersive spectrometer attached to an SEM (JSM-7500F + EDS, Oxford, U.K.). The phase of the samples was analyzed by high-resolution X-ray diffraction (XRD, X'Pert PRO Multi-Purpose X-ray Diffractometer) using Cu kW at 50 mA and 60 kV. The chemical bond structures were examined by a Fourier transform infrared (FT-IR, Spectrum 400) spectrometer.

Mechanical Property of Tendon-Inspired Patch. The mechanical properties (*i.e.*, stress and elongation) of the flat and tendon-inspired patch (diameter: 20 mm) were measured using an MCT-1150 tensile tester (A&D Company, Japan) at a cross-head speed of 100 mm/min. The tendon-inspired patches were analyzed by applying load along the direction of aligned nanotopography. The sample was measured at a cross-head distance of 0.25 mm from the center of the sample. Ten specimens were analyzed for each sample. The peak load and displacement at the breaking point were recorded.

Isolation and Culturing of Human Tendon-Derived Cells. The tendon tissue samples were collected from normal supraspinatus tendon out of damaged tendon tissue of patients during arthroscopic RC repairs under sufficient informed consent at Chonnam National University Medical School and Chonnam National University Hospital. Tendon tissue samples were washed with phosphonate-buffered saline (PBS), cut into small pieces, and digested with 3 mg/mL collagenase type I (Sigma) in Dulbecco's modified Eagle's medium (DMEM) at 37 °C for 16 h. After enzymatic digestion, equal volumes of DMEM were added to quench the collagenase and filtered through cell strainers (70 μm size). The filtered cell suspension was centrifuged at 1500 rpm for 5

https://dx.doi.org/10.1021/acsomega.0c01328
ACS Omega 2020, 5, 13913−13925

min. The cell pellets were resuspended and cultured in Dulbecco's modified Eagle's medium (DMEM low glucose: Gibco) supplemented with 10% fetal bovine serum (FBS) and 1% penicillin−streptomycin at 37 °C in a 5% CO_2 atmosphere. The medium was changed every 3 days. All cells used in this work were at passage 3 or 4. The morphological characteristics of isolated human tendon-derived cells were confirmed by an optical microscope. The tendon-derived cells have the spindle morphology with multiple long cytoplasmic processes forming cell−cell contacts (Figure S3).[52−55]

SEM Observation of Tendon-Derived Cells. The detailed method has already been reported by our group.[28] The morphologies of tendon-derived cells adhered on tendon-inspired patch were observed by a field emission scanning electron microscope (FE-SEM). Tendon-derived cells were seeded at a density of 1×10^4 cells/sample. After 3 days of cell seeding, cells that adhered onto the sample surfaces were fixed with modified Karnovsky's fixative consisting of 2% paraformaldehyde and 2% glutaraldehyde (Sigma-Aldrich) in a 0.05 M sodium cacodylate buffer (Sigma-Aldrich) at 4 °C for 4 h. The samples were washed three times with 0.05 M sodium cacodylate buffer for 10 min and fixed with 1% osmium tetroxide (Sigma-Aldrich) at room temperature for 100 min in the dark. The samples were then washed with distilled water and dehydrated with graded concentrations (50, 70, 80, 90, and 100% v/v) of ethanol. The samples were then treated with hexamethyldisilazane (Sigma-Aldrich) for 30 min twice and dried in air overnight in the dark. Finally, the samples were coated with platinum prior to cell shape observation with an FE-SEM (JSM-7500F, Oxford, U.K.).

Immunofluorescence Staining. The detailed method has already been reported by our group. Adhered cells on samples were fixed with a 4% paraformaldehyde solution (Sigma-Aldrich, Milwaukee, WI) for 20 min, permeabilized with 0.1% Triton X-100 (Sigma-Aldrich, WI, Milwaukee) for 15 min, and stained with TRITC-conjugated phalloidin (Millipore, Billerica, MA) for 1 h and 4,6-diamidino-2-phenylindole (DAPI; Millipore, Billerica, MA) for 5 min. After each process, the samples were washed three times with 1× PBS for 5 min each. The images of the stained cells were taken using a fluorescence microscope (Zeiss, Germany).

Cell Attachment and Proliferation Analysis. Tendon-derived cells (1×10^4 cells/samples) were seeded onto the samples and cultured for 6 h (cell attachment) and 5 days in Dulbecco's modified Eagle's medium (DMEM) (Cellgro) containing 10% fetal bovine serum (FBS) (Cellgro) and 1% antibiotics (Cellgro) at 37 °C in a humidified atmosphere containing 5% CO_2. The quantitative analysis of the cell attachment and proliferation on the scaffolds was performed using a WST-1 assay (Premix WST-1 Cell Proliferation Assay System, Takara Bio, Inc., Japan). To confirm the cell attachments, the cells on the scaffolds after 6 h culture were washed using PBS to remove the cells not attached onto the scaffolds prior to the quantitative analysis using WST-1 assay.

Western Blot Analysis. The detailed method has already been reported by our group. Total cellular proteins were extracted by RIPA Cell Lysis buffer (GenDEPOT, Huston, TX) with added Xpert proteinase inhibitor cocktail (GenDEPOT, Huston, TX). Cell lysates were incubated on ice for 30 min and then centrifuged at 12 000 rpm for 30 min at 4 °C. Protein concentrations were determined by the bicinchonic acid method (BCA kit) (Pierce, IL). Equal amounts of proteins of cell lysates were electrophoresed in 10% sodium dodecyl sulfate−polyacrylamide gel using a Bio-Rad MiniProtean (Bio-Rad, CA) gel apparatus, and the electrophoresed gel slabs were electrotransferred to poly(vinylidene difluoride) (PVDF) membranes (Amersham Life Science, U.K.) at 4 °C in transfer buffer (30 mM Tris, 240 mM glycine, 25% methanol) at a constant voltage of 100 V for 1 h. The membrane was blocked in 5% skim milk powder in TBS-T, pH 7.6 (100 mM Tris buffer with 150 mM NaCl and 0.1% Tween 20), and the blot was incubated with the specific primary antibodies. To detect collagen type I, collagen type III, osteocalcin, fibronectin, and β-actin, we used monoclonal antibodies (Santa Cruz Biotechnology, CA) at a final concentration in blocking buffer of 1 μg/mL (1:1000 dilution). HRP-goat anti-mouse immunoglobulin (Invitrogen, IL) was used as the secondary antibody at a dilution of 1:2000 for 1 h at room temperature, and then the membrane was similarly washed five times for 5 min each in TBS-T. Bands were detected using the Immobilon Western Chemiluminescent HRP substrate (Millipore, MA, U.K.). Quantification of the western blot was performed using the NineAlliance (UVItec, Cambridge, U.K.) software with a normalization of the level of the entire protein. The quantification of the western blot band intensity was measured using ImageJ software.

Osteogenic Mineralization Analysis. The detailed method has already been reported by our group. Tendon-derived cells (4×10^4 cells/sample) were cultured for 14 days on the samples in osteogenic differentiation medium (100 nM dexamethasone, 50 μm ascorbic acid, and 10 mm glycerol 2-phosphate in normal media). Alizarin Red S (Sigma-Aldrich) staining was used to confirm the osteogenic differentiation of tendon-derived cells on the sample surfaces. The degree of mineralization was measured by staining tendon-derived cells cultured on the sample surfaces with Alizarin Red S. The stained cells were destained with cetylpyridinium chloride (Sigma-Aldrich), and the extracted stains were then measured using an Absorbance reader (iMark Microplate Absorbance Reader, Bio-Rad, Hercules) at 595 nm to quantify the osteogenic differentiation of tendon-derived cells.

Wound Healing Analysis. A thin PDMS slab was utilized to generate a cell-free area for investigating migration and wound healing effects of tendon-derived cells on the samples. Specifically, a 200 μm thick PDMS sheet was cut into slabs with a width of 800 μm and a length of 20 mm using two intact sharp blades. The PDMS slabs were placed onto the tendon-inspired patch surface vertically along the nanopattern direction. Tendon-derived cells (1×10^5 cells/samples) were cultured on the wound generation samples. Then, PDMS slabs were removed manually with sharp tweezers and the cells of wound healing system were observed at 0, 12, 24, and 36 h by immunofluorescence staining using a fluorescence microscope (Zeiss, Germany). The data of cell-covered area and migration speed in wound healing analysis were investigated using ImageJ software.

***In Vivo* Animal Study of Acute and Chronic Animal Model.** The animal studies were approved by the Ethics Committee of Chonnam National University Medical School and Chonnam National University Hospital (CNU IACUC-H-2016-33) and were performed in accordance with relevant guidelines and regulations. Twelve New Zealand white rabbits weighing 2.8−3.2 kg were used and divided into native tendon tissue group, nonpatch group, flat patch group, and tendon-inspired patch group. Rabbits were fully anesthetized with an intramuscular injection of 35 mg/kg ketamine (Youhan

https://dx.doi.org/10.1021/acsomega.0c01328
ACS Omega 2020, 5, 13913−13925

Corporation, Seoul, Korea) and 5 mg/kg xylazine hydrochloride (Rompun; Bayer HealthCare, Korea). Both shoulders of each rabbit were shaved and disinfected with povidone-iodine (Firson, Korea), and the animals were placed in lateral position with the forelimbs in adduction and external rotation. A 3.0 cm skin incision over the scapulohumeral joint was made, subcutaneous tissue was dissected, and omotransverse and trapezius muscles were retracted to expose supraspinatus tendon (located in a superior position to the scapular spine). A sharp release of the supraspinatus tendon at a greater tuberosity of the humerus over a 10 mm width was observed for the acute RC tear model, and a surgical RC repair was performed immediately after the supraspinatus tendon tear. We used the right shoulder for tendon-inspired patch application (n = 6) and the left shoulder for flat patch application (n = 6). For chronic RC tear model, we wrapped the detached tendon stump with silicone Penrose drain with 10 mm long and 8 mm outer diameter (Yushin Corp, Bucheon, Korea) to prevent adhesion to the surrounding soft tissue for 4 weeks until the secondary procedures could be performed. We used the left shoulder as native the tendon tissue group (n = 3) and the nonpatch group (n = 3) and the right shoulder as the flat patch (n = 3) group and the tendon-inspired patch (n = 3) group. The fascia and subcutaneous tissues were sutured using interrupted 3−0 vicryl sutures (Ethicon, Johnson & Johnson), and the skin was sutured with interrupted 4−0 prolene sutures. All rabbits tolerated this procedure without any intraoperative complications. After surgery, analgesis and antibiotic (enrofloxacin, 1 mg/mL, Bayer, Germany) intramuscular injection were administered. The shoulders were not immobilized postoperatively. The rabbits were housed individually and had free access to water and food. With regard to the RC repair technique, the torn supraspinatus tendon was repaired with 2.0 Ticron (Tyco, Waltham) in a transosseous manner after creating a bleeding bed at the footprint of the greater tuberosity. Two bone tunnels were created at the articular margin of the footprint to the lateral humeral cortex. The suture was passed through the bone tunnels and tied, reattaching the supraspinatus tendon to the footprint. The flat patches and tendon-inspired patches were used to augment the repair site by stitching the proximal portion of the patch to the supraspinatus tendon and the distal portion to the soft tissue at the lateral portion of the proximal humerus.

Histological Observations and Evaluation. The proximal humerus including the greater tuberosity head with attached supraspinatus tendon of both the shoulders of each rabbit was harvested. Specimens were fixed in neutral buffered 10% formalin (pH 7.4) and decalcified with Calci-Clear Rapid (National Diagnostics, Atlanta) for 2 weeks, and paraffin blocks were made in the repair site including supraspinatus tendon and greater tuberosity. Sections (4 μm thickness) were cut in the coronal plane and stained with hematoxylin and eosin (H&E), Masson's trichrome. We assessed vascularity, cellularity, collagen fiber continuity, orientation, density, and maturation of the tendon-to-bone interface, and we also evaluated the inflammation rate around patch at the tendon-to-patch interface. Images were captured and acquired using Aperio ImageScope (Leica, CA) software. Collagen proteins were then stained using a Picrosirius red staining kit (ab150681, Abcam, Cambridge, MA) following the manufacturer's instruction. Briefly, a Sirius red dye solution was added to completely immerse the fixed tissues and incubated for 60 min at room temperature. After removing the dye solution, the samples were rinsed twice with 0.5% acetic acid solution and then three times with absolute alcohol to dehydrate the sample. For viewing type I and type III collagen, polarizing lenses were used on a microscope (Olympus BX53) and photos were taken using attached capture software Focus Lite ver2.90 (Focus company). General histological evaluation was performed with hematoxylin and eosin (200× magnification), Masson's trichrome (200× magnification), and Picrosirius red (100× magnification) stained slides of chronic RC tear animal models. The slides were evaluated using the semiquantitative grading scale of the Bonar score, which assesses four variables (cell morphology, ground substance, collagen arrangement, and vascularity) of tendon-to-bone interfaces. A four-point scoring system is used, where 0 indicates a normal appearance and 3 indicates a markedly abnormal appearance (Table S1).[56−58] The total histological scores for each group were calculated from the sum of these four characteristic grades. Four sections were randomly selected from each group and were evaluated blindly by three independent assessors. The average score was used for comparison.

Statistical Analysis. All quantitative results are presented as mean ± standard deviation (SD), and unpaired Student's t-tests were used for statistical analysis. Statistical analyses of the histological scores were performed using Kruskal−Wallis testing with SPSS software.

■ ASSOCIATED CONTENT

Supporting Information

The Supporting Information is available free of charge at https://pubs.acs.org/doi/10.1021/acsomega.0c01328.

Histological evaluation grade; Distribution of histologic scores; Young's modulus, breakpoint stress, breakpoint strain of the flat patch, and tendon-inspired patch; quantification of the western blot band intensity; Western blot band intensity was used to measure expression differences of collagen type I, collagen type III, osteocalcin, and fibronectin on the flat and tendon-inspired patches; and image of the isolated human tenocytes (PDF)

■ AUTHOR INFORMATION

Corresponding Authors

Myung-Sun Kim − *Department of Orthopedics, Chonnam National University Hospital, Gwangju 61649, Republic of Korea*; Email: mskim@chonnam.ac.kr

Jangho Kim − *Department of Rural and Biosystems Engineering, Chonnam National University, Gwangju 61186, Republic of Korea*; orcid.org/0000-0001-9424-8215; Email: rain2000@jnu.ac.kr

Authors

Woochan Kim − *Department of Rural and Biosystems Engineering, Chonnam National University, Gwangju 61186, Republic of Korea*

Ga-Eon Kim − *Department of Pathology, Chonnam National University Hospital, Gwangju 61649, Republic of Korea*

Mohamed Attia Abdou − *Department of Orthopedics, Chonnam National University Hospital, Gwangju 61649, Republic of Korea*

Sujin Kim − *Department of Rural and Biosystems Engineering, Chonnam National University, Gwangju 61186, Republic of Korea*

https://dx.doi.org/10.1021/acsomega.0c01328
ACS Omega 2020, 5, 13913−13925

Daun Kim − *Department of Rural and Biosystems Engineering, Chonnam National University, Gwangju 61186, Republic of Korea*
Sunho Park − *Department of Rural and Biosystems Engineering, Chonnam National University, Gwangju 61186, Republic of Korea*
Yang-Kyung Kim − *Department of Orthopedics, Chonnam National University Hospital, Gwangju 61649, Republic of Korea*
Yonghyun Gwon − *Department of Rural and Biosystems Engineering, Chonnam National University, Gwangju 61186, Republic of Korea*
Sung-Eun Jeong − *Department of Orthopedics, Chonnam National University Hospital, Gwangju 61649, Republic of Korea*

Complete contact information is available at:
https://pubs.acs.org/10.1021/acsomega.0c01328

Author Contributions

J.K. and M.-S.K. supervised the project. W.K., G.-E.K., D.K., S.P., Y.-K.K., M.-S.K., and J.K. conceived and designed the experiments on research. W.K., D.K., S.P., Y.G., S.K., M.A.A., Y.-K.K., and S.J. carried out the experiments. W.K., G.-E.K., D.K., S.P., S.J., and Y.-K.K. analyzed the results on the experiments. W.K., G.-E.K., D.K., S.P., Y.-K.K., M.-S.K., and J.K. discussed the results in detail. W.K., D.K., S.P., Y.-K.K., M.-S.K., and J.K. wrote the manuscript.

Notes

The authors declare no competing financial interest.

■ ACKNOWLEDGMENTS

This work was supported by the National Research Foundation of Korea (NRF) grant funded by the Korea government (NRF-2016M3A9B4919353).

■ REFERENCES

(1) Maffulli, N.; Longo, U. G.; Loppini, M.; Berton, A.; Spiezia, F.; Denaro, V. Tissue Engineering for Rotator Cuff Repair: An Evidence-Based Systematic Review. *Stem Cells Int.* **2012**, No. 418086.
(2) Baker, A. R.; McCarron, J. A.; Tan, C. D.; Iannotti, J. P.; Derwin, K. A. Does Augmentation with a Reinforced Fascia Patch Improve Rotator Cuff Repair Outcomes? *Clin. Orthop. Relat. Res.* **2012**, *470*, 2513−2521.
(3) Beason, D. P.; Connizzo, B. K.; Dourte, L. M.; Mauck, R. L.; Soslowsky, L. J.; Steinberg, D. R.; Bernstein, J. Fiber-aligned polymer scaffolds for rotator cuff repair in a rat model. *J. Shoulder Elbow Surg.* **2012**, *21*, 245−250.
(4) Shea, K. P.; Obopilwe, E.; Sperling, J. W.; Iannotti, J. P. A biomechanical analysis of gap formation and failure mechanics of a xenograft-reinforced rotator cuff repair in a cadaveric model. *J. Shoulder Elbow Surg.* **2012**, *21*, 1072−1079.
(5) Calvert, P.; Packer, N.; Stoker, D.; Bayley, J.; Kessel, L. Arthrography of the shoulder after operative repair of the torn rotator cuff. *J. Bone Jt. Surg., Br. Vol.* **1986**, *68*, 147−150.
(6) Harryman, D.; Mack, L.; Wang, K.; Jackins, S.; Richardson, M.; Matsen, F. Repairs of the rotator cuff. Correlation of functional results with. *J. Bone Jt. Surg.* **1991**, *73*, 982−989.
(7) Liu, S. H.; Baker, C. L. Arthroscopically assisted rotator cuff repair: correlation of functional results with integrity of the cuff. *Arthroscopy* **1994**, *10*, 54−60.
(8) Galatz, L. M.; Ball, C. M.; Teefey, S. A.; Middleton, W. D.; Yamaguchi, K. The outcome and repair integrity of completely arthroscopically repaired large and massive rotator cuff tears. *J. Bone Jt. Surg.* **2004**, *86*, 219−224.
(9) Longo, U. G.; Lamberti, A.; Khan, W. S.; Maffulli, N.; Denaro, V. Synthetic Augmentation for Massive Rotator Cuff Tears. *Sports Med. Arthrosc. Rev.* **2011**, *19*, 360−365.
(10) Shepherd, H. M.; Lam, P. H.; Murrell, G. A. C. Biomechanics of Synthetic Patch Rotator Cuff Repairs. *Tech. Shoulder Elbow Surg.* **2011**, *12*, 94−100.
(11) Aurora, A.; McCarron, J. A.; van den Bogert, A. J.; Gatica, J. E.; Iannotti, J. P.; Derwin, K. A. The biomechanical role of scaffolds in augmented rotator cuff tendon repairs. *J. Shoulder Elbow Surg.* **2012**, *21*, 1064−1071.
(12) McCarron, J. A.; Milks, R. A.; Mesiha, M.; Aurora, A.; Walker, E.; Iannotti, J. P.; Derwin, K. A. Reinforced fascia patch limits cyclic gapping of rotator cuff repairs in a human cadaveric model. *J. Shoulder Elbow Surg.* **2012**, *21*, 1680−1686.
(13) Min, H. K.; Kwon, O. S.; Oh, S. H.; Lee, J. H. Platelet-derived growth factor-BB-immobilized asymmetrically porous membrane for enhanced rotator cuff tendon healing. *Tissue Eng. Regener. Med.* **2016**, *13*, 568−578.
(14) Zhang, C.; Liu, Y. J. Biomechanic and histologic analysis of fibroblastic effects of tendon-to-bone healing by transforming growth factor beta 1 (TGF-beta 1) in rotator cuff tears. *Acta Cir. Bras.* **2017**, *32*, 1045−1055.
(15) Kim, Y. S.; Lee, H. J.; Ok, J. H.; Park, J. S.; Kim, D. W. Survivorship of implanted bone marrow-derived mesenchymal stem cells in acute rotator cuff tear. *J. Shoulder Elbow Surg.* **2013**, *22*, 1037−1045.
(16) Mora, M. V.; Iban, M. A. R.; Heredia, J. D.; Laakso, R. B.; Cuellar, R.; Arranz, M. G. Stem cell therapy in the management of shoulder rotator cuff disorders. *World J. Stem Cells* **2015**, *7*, 691−699.
(17) Peterson, D. R.; Ohashi, K. L.; Aberman, H. M.; Piza, P. A.; Crockett, H. C.; Fernandez, J. I.; Lund, P. J.; Funk, K. A.; Hawes, M. L.; Parks, B. G.; Mattern, R. H. Evaluation of a collagen-coated, resorbable fiber scaffold loaded with a peptide basic fibroblast growth factor mimetic in a sheep model of rotator cuff repair. *J. Shoulder Elbow Surg.* **2015**, *24*, 1764−1773.
(18) Nowotny, J.; Aibibu, D.; Farack, J.; Nimtschke, U.; Hild, M.; Gelinsky, M.; Kasten, P.; Cherif, C. Novel fiber-based pure chitosan scaffold for tendon augmentation: biomechanical and cell biological evaluation. *J. Biomater. Sci., Polym. Ed.* **2016**, *27*, 917−936.
(19) Zheng, Z. F.; Ran, J. S.; Chen, W. S.; Hu, Y. J.; Zhu, T.; Chen, X.; Yin, Z.; Heng, B. C.; Feng, G.; Le, H. H.; Tang, C. Q.; Huang, J. Y.; Chen, Y. W.; Zhou, Y. T.; Dominique, P.; Shen, W. L.; Ouyang, H. W. Alignment of collagen fiber in knitted silk scaffold for functional massive rotator cuff repair. *Acta Biomater.* **2017**, *51*, 317−329.
(20) Chung, S. W.; Song, B. W.; Kim, Y. H.; Park, K. U.; Oh, J. H. Effect of Platelet-Rich Plasma and Porcine Dermal Collagen Graft Augmentation for Rotator Cuff Healing in a Rabbit Model. *Am. J. Sports Med.* **2013**, *41*, 2909−2918.
(21) Sun, Y. Y.; Han, F.; Zhang, P.; Zhi, Y. L.; Yang, J. J.; Yao, X. H.; Wang, H.; Lin, C.; Wen, X. J.; Chen, J. W.; Zhao, P. A synthetic bridging patch of modified co-electrospun dual nano-scaffolds for massive rotator cuff tear. *J. Mater. Chem. B* **2016**, *4*, 7259−7269.
(22) Lipner, J.; Shen, H.; Cavinatto, L.; Liu, W. Y.; Havlioglu, N.; Xia, Y. N.; Galatz, L. M.; Thomopoulos, S. In Vivo Evaluation of Adipose-Derived Stromal Cells Delivered with a Nanofiber Scaffold for Tendon-to-Bone Repair. *Tissue Eng., Part A* **2015**, *21*, 2766−2774.
(23) Ricchetti, E. T.; Aurora, A.; Iannotti, J. P.; Derwin, K. A. Scaffold devices for rotator cuff repair. *J. Shoulder Elbow Surg.* **2012**, *21*, 251−265.
(24) Ratcliffe, A.; Butler, D. L.; Dyment, N. A.; Cagle, P. J.; Proctor, C. S.; Ratcliffe, S. S.; Flatow, E. L. Scaffolds for Tendon and Ligament Repair and Regeneration. *Ann. Biomed. Eng.* **2015**, *43*, 819−831.
(25) Chainani, A.; Little, D. Current Status of Tissue-engineered Scaffolds for Rotator Cuff Repair. *Tech. Orthop.* **2016**, *31*, 91−97.
(26) Kim, J.; Kim, H. N.; Lim, K.-T.; Kim, Y.; Seonwoo, H.; Park, S. H.; Lim, H. J.; Kim, D.-H.; Suh, K.-Y.; Choung, P.-H.; Choung, Y.-H.; Chung, J. H. Designing nanotopographical density of extracellular matrix for controlled morphology and function of human mesenchymal stem cells. *Sci. Rep.* **2013**, *3*, No. 3552.

(27) Kim, J.; Won-Gyu, B.; Ju, K. Y.; Hoon, S.; Han-Wool, C.; Kyoung-Je, J.; Sunho, P.; Hee, K. B.; Hong-Nam, K.; Soon, C. K.; Myung-Sun, K.; Pill-Hoon, C.; Yun-Hoon, C.; Hoon, C. J. Directional Matrix Nanotopography with Varied Sizes for Engineering Wound Healing. *Adv. Healthcare Mater.* **2017**, *6*, No. 1700297.
(28) Kim, J.; Kim, H. N.; Lim, K.-T.; Kim, Y.; Pandey, S.; Garg, P.; Choung, Y.-H.; Choung, P.-H.; Suh, K.-Y.; Chung, J. H. Synergistic effects of nanotopography and co-culture with endothelial cells on osteogenesis of mesenchymal stem cells. *Biomaterials* **2013**, *34*, 7257−7268.
(29) Kim, H. N.; Hong, Y.; Kim, M. S.; Kim, S. M.; Suh, K.-Y. Effect of orientation and density of nanotopography in dermal wound healing. *Biomaterials* **2012**, *33*, 8782−8792.
(30) Kim, D.-H.; Provenzano, P. P.; Smith, C. L.; Levchenko, A. Matrix nanotopography as a regulator of cell function. *J. Cell Biol.* **2012**, *197*, 351−360.
(31) Kim, H. N.; Jiao, A.; Hwang, N. S.; Kim, M. S.; Kang, D. H.; Kim, D.-H.; Suh, K.-Y. Nanotopography-guided tissue engineering and regenerative medicine. *Adv. Drug Delivery Rev.* **2013**, *65*, 536−558.
(32) Park, S.; Choi, K. S.; Kim, W.; Lee, D.; Kim, D.; Kim, M.-S.; Kim, K.; Kim, J. Engineering nanowrinkled microfibers composed of eggshell membrane and graphene. *Mater. Lett.* **2018**, 78−81.
(33) Park, S.; Choi, K. S.; Kim, D.; Kim, W.; Lee, D.; Kim, H.-N.; Hyun, H.; Lim, K.-T.; Kim, J.-W.; Kim, Y.-R.; Kim, J. Controlled extracellular topographical and chemical cues for acceleration of neuronal development. *J. Ind. Eng. Chem.* **2018**, *61*, 65−70.
(34) Kim, J.; Kim, H. N.; Lim, K.-T.; Kim, Y.; Seonwoo, H.; Park, S. H.; Lim, H. J.; Kim, D.-H.; Suh, K.-Y.; Choung, P.-H.; et al. Designing nanotopographical density of extracellular matrix for controlled morphology and function of human mesenchymal stem cells. *Sci. Rep.* **2013**, *3*, No. 3552.
(35) Kim, J.; Bae, W. G.; Kim, Y. J.; Seonwoo, H.; Choung, H. W.; Jang, K. J.; Park, S.; Kim, B. H.; Kim, H. N.; Choi, K. S.; et al. Directional matrix nanotopography with varied sizes for engineering wound healing. *Adv. Healthcare Mater.* **2017**, *6*, No. 1700297.
(36) Kannus, P. Structure of the tendon connective tissue. *Scand. J. Med. Sci. Sports* **2000**, *10*, 312−320.
(37) Kleiner, D. M. Human tendons: anatomy, physiology and pathology. *J. Athl. Train.* **1998**, *33*, 185.
(38) Bae, W.-G.; Kim, J.; Choung, Y.-H.; Chung, Y.; Suh, K. Y.; Pang, C.; Chung, J. H.; Jeong, H. E. Bio-inspired configurable multiscale extracellular matrix-like structures for functional alignment and guided orientation of cells. *Biomaterials* **2015**, *69*, 158−164.
(39) Zhang, X. Z.; Bogdanowicz, D.; Erisken, C.; Lee, N. M.; Lu, H. H. Biomimetic scaffold design for functional and integrative tendon repair. *J. Shoulder Elbow Surg.* **2012**, *21*, 266−277.
(40) Abdou, M. A.; Kim, G.-E.; Kim, J.; Kim, B.-H.; Kim, Y.-K.; Jeong, S.-E.; Kim, T.-J.; Park, H.-K.; Kim, M.-S. How Long Should We Wait to Create the Goutallier Stage 2 Fatty Infiltrations in the Rabbit Shoulder for Repairable Rotator Cuff Tear Model? *BioMed. Res. Int.* **2019**, *2019*, 1−11.
(41) Chainani, A.; Little, D. Current status of tissue-engineered scaffolds for rotator cuff repair. *Tech. Orthop.* **2016**, *31*, 91.
(42) Derwin, K.; Baker, A.; Spragg, R.; Leigh, D.; Iannotti, J. Commercial extracellular matrix scaffolds for rotator cuff tendon repair: biomechanical, biochemical, and cellular properties. *J. Bone Jt. Surg., Am. Vol.* **2006**, *88*, 2665−2672.
(43) Aurora, A.; McCarron, J.; Iannotti, J.; Derwin, K. Commercially available extracellular matrix materials for rotator cuff repairs: State of the art and future trends. *J. Shoulder Elbow Surg.* **2007**, *16*, S171−S178.
(44) Zhang, X.; Bogdanowicz, D.; Erisken, C.; Lee, N. M.; Lu, H. H. Biomimetic scaffold design for functional and integrative tendon repair. *J. Shoulder Elbow Surg.* **2012**, *21*, 266−277.
(45) Derwin, K. A.; Badylak, S. F.; Steinmann, S. P.; Iannotti, J. P. Extracellular matrix scaffold devices for rotator cuff repair. *J. Shoulder Elbow Surg.* **2010**, *19*, 467−476.
(46) Sun, Y.; Han, F.; Zhang, P.; Zhi, Y.; Yang, J.; Yao, X.; Wang, H.; Lin, C.; Wen, X.; Chen, J.; Zhao, P. A synthetic bridging patch of modified co-electrospun dual nano-scaffolds for massive rotator cuff tear. *J. Mater. Chem. B* **2016**, *4*, 7259−7269.
(47) Lipner, J.; Shen, H.; Cavinatto, L.; Liu, W.; Havlioglu, N.; Xia, Y.; Galatz, L. M.; Thomopoulos, S. In vivo evaluation of adipose-derived stromal cells delivered with a nanofiber scaffold for tendon-to-bone repair. *Tissue Eng., Part A* **2015**, *21*, 2766−2774.
(48) Bagherzadeh, R.; Latifi, M.; Kong, L. Three-dimensional pore structure analysis of polycaprolactone nano-microfibrous scaffolds using theoretical and experimental approaches. *J. Biomed. Mater. Res., Part A* **2014**, *102*, 903−910.
(49) Kim, J.; Bae, W.-G.; Choung, H.-W.; Lim, K. T.; Seonwoo, H.; Jeong, H. E.; Suh, K.-Y.; Jeon, N. L.; Choung, P.-H.; Chung, J. H. Multiscale patterned transplantable stem cell patches for bone tissue regeneration. *Biomaterials* **2014**, *35*, 9058−9067.
(50) Peach, M. S.; Ramos, D. M.; James, R.; Morozowich, N. L.; Mazzocca, A. D.; Doty, S. B.; Allcock, H. R.; Kumbar, S. G.; Laurencin, C. T. Engineered stem cell niche matrices for rotator cuff tendon regenerative engineering. *PLoS One* **2017**, *12*, No. e0174789.
(51) Sevivas, N.; Teixeira, F. G.; Portugal, R.; Direito-Santos, B.; Espregueira-Mendes, J.; Oliveira, F. J.; Silva, R. F.; Sousa, N.; Sow, W. T.; Nguyen, L. T. H.; Ng, K. W.; Salgado, A. J. Mesenchymal Stem Cell Secretome Improves Tendon Cell Viability In Vitro and Tendon-Bone Healing In Vivo When a Tissue Engineering Strategy Is Used in a Rat Model of Chronic Massive Rotator Cuff Tear. *Am. J. Sports Med.* **2018**, *46*, 449−459.
(52) Chiu, C.-H.; Lei, K. F.; Yeh, W.-L.; Chen, P.; Chan, Y.-S.; Hsu, K.-Y.; Chen, A. C.-Y. Comparison between xCELLigence biosensor technology and conventional cell culture system for real-time monitoring human tenocytes proliferation and drugs cytotoxicity screening. *J. Orthop. Surg. Res.* **2017**, *12*, 149.
(53) Schulze-Tanzil, G.; Al-Sadi, O.; Wiegand, E.; Ertel, W.; Busch, C.; Kohl, B.; Pufe, T. The role of pro-inflammatory and immunoregulatory cytokines in tendon healing and rupture: new insights. *Scand. J. Med. Sci. Sports* **2011**, *21*, 337−351.
(54) Yao, L.; Bestwick, C.; Bestwick, L. A.; Maffulli, N.; Aspden, R. M. Phenotypic drift in human tenocyte culture. *Tissue Eng.* **2006**, *12*, 1843−1849.
(55) Schulze-Tanzil, G.; Mobasheri, A.; Clegg, P.; Sendzik, J.; John, T.; Shakibaei, M. Cultivation of human tenocytes in high-density culture. *Histochem. Cell Biol.* **2004**, *122*, 219−228.
(56) Cook, J.; Feller, J.; Bonar, S.; Khan, K. Abnormal tenocyte morphology is more prevalent than collagen disruption in asymptomatic athletes' patellar tendons. *J. Orthop. Res.* **2004**, *22*, 334−338.
(57) Fearon, A.; Dahlstrom, J. E.; Twin, J.; Cook, J.; Scott, A. The Bonar score revisited: region of evaluation significantly influences the standardized assessment of tendon degeneration. *J. Sci. Med. Sport* **2014**, *17*, 346−350.
(58) Khan, K. M.; Cook, J. L.; Bonar, F.; Harcourt, P.; Åstrom, M. Histopathology of common tendinopathies. *Sports Med.* **1999**, *27*, 393−408.

https://dx.doi.org/10.1021/acsomega.0c01328
ACS Omega 2020, 5, 13913−13925